Research in Astronomy and Astrophysics, 23:015015 (10pp), 2023 January https://doi.org/10.1088/1674-4527/aca505


# Broadband Spectral Properties of MAXI J1348–630 using AstroSat Observations

Gitika Mall[1], Jithesh Vadakkumthani[2], and Ranjeev Misra[3]
[1] Center for Field Theory and Particle Physics and Department of Physics, Fudan University, Shanghai 200438, China; gitikamall20@fudan.edu.cn
[2] Department of Physics and Electronics, CHRIST (Deemed to be University), Hosur Main Road, Bengaluru 560029, India
[3] Inter-University Centre for Astronomy and Astrophysics (IUCAA), PB No.4, Ganeshkhind, Pune 411007, India
*Received 2022 June 30; revised 2022 October 28; accepted 2022 November 7; published 2022 December 21*

## Abstract

We present broadband X-ray spectral analysis of the black hole X-ray binary MAXI J1348–630, performed using five AstroSat observations. The source was in the soft spectral state for the first three observations and in the hard state for the last two. The three soft state spectra were modeled using a relativistic thin accretion disk with reflection features and thermal Comptonization. Joint fitting of the soft state spectra constrained the spin parameter of the black hole $a_* > 0.97$ and the disk inclination angle $i = 32.9^{+4.1}_{-0.6}$ degrees. The bright and faint hard states had bolometric flux a factor of ∼6 and ∼10 less than that of the soft state respectively. Their spectra were fitted using the same model except that the inner disk radius was not assumed to be at the last stable orbit. However, the estimated values do not indicate large truncation radii and the inferred accretion rate in the disk was an order of magnitude lower than that of the soft state. Along with earlier reported temporal analysis, AstroSat data provide a comprehensive picture of the evolution of the source.

*Key words:* black hole physics – X-rays: binaries – accretion – accretion disks – X-rays: individual (MAXI J1348–630)

## 1. Introduction

Transient X-ray binaries, particularly black hole X-ray binaries (BHXRBs), spend long periods in quiescence and occasionally exhibit outbursts typically lasting from weeks to a few months. During the outburst, transitions between various X-ray spectral states accompanied by variations in spectral properties are observed (Homan & Belloni 2005). These states, characterized by luminosities and spectral shapes, are primarily of two types: Low Hard State (LHS) and High Soft State (HSS). There are also intermediate states. Typically, in the rising phase of the outburst, the source evolves from LHS to Hard-Intermediate State followed by Soft-Intermediate State (SIMS) and finally to HSS (Homan & Belloni 2005; Remillard & McClintock 2006; Belloni 2009). During the decaying phase of the outburst, the source returns to LHS from HSS via intermediate state (Homan & Belloni 2005; van der Klis 2006; Motta et al. 2011; Muñoz-Darias et al. 2011).

In the soft state, the X-ray flux is dominated by thermal emission from an optically thick and geometrically thin accretion disk (the standard disk; Shakura & Sunyaev 1973). This observed spectrum can be reproduced with a multi-color disk model (Mitsuda et al. 1984). The inner disk radius remains constant in this state irrespective of significant changes in X-ray luminosity and temperature (e.g., Ebisawa et al. 1993; Kubota & Makishima 2004; Steiner et al. 2010; Shidatsu et al. 2011). This implies that the standard disk extends down to the innermost stable circular orbit (ISCO). Since the inner edge of the disk is close to the black hole, the observed disk blackbody spectra can be fundamentally altered by Doppler shifting and relativistic effects (Gierlinski & Done 2004). The resulting spectral shape depends strongly on the viewing angle to the source (Muñoz-Darias et al. 2013). In this state, the disk spectrum is prominent enough to measure the spin of the compact object using the continuum-fitting method. This is done by estimating the inner radius ($R_{\rm in}$) of the accretion disk and identifying it with the radius of ISCO ($R_{\rm ISCO}$). $R_{\rm ISCO}$ is a monotonic function of the dimensionless black hole spin parameter $a_*$, decreasing from 6 $r_g$ to 1.235 $r_g$ (where $r_g$ is gravitational radius in units of $GM/c^2$) as spin increases from $a_* = 0$ to $a_* = 1$ (Bardeen et al. 1972). This relationship between $a$ and $R_{\rm ISCO}$ allows for estimating the spin parameter by continuum-fitting method (Zhang et al. 1997; Gou et al. 2011). A complementary method for spin measurement is to use the shape of the relativistically modified fluorescence iron line emission, which depends on the disk inclination angle (Fabian et al. 1989; Reynolds & Nowak 2003).

In the hard state, the energy spectra are dominated by a strong Comptonized emission from the hot cloud of electrons known as the "corona" (Petrucci 2008) and the source exhibits a hard power law shaped X-ray spectrum with an index ∼1.7. Moreover, the disk appears much cooler compared to the soft state and is believed to be truncated at a large radius from the

compact object (Remillard & McClintock 2006). The quasi-steady jets are often associated with this state and clear correlations between the radio and X-ray intensities are observed (Remillard & McClintock 2006; Belloni 2009). However, contrary to the truncated disk model, in a few cases, the disk has been found to extend close to the black hole in the hard state, when the source luminosity is greater than a few per cent of the Eddington luminosity (Shidatsu et al. 2014). For example, modeling the reflection spectra of GX 339–4 in two extreme spectral states, Reis et al. (2008) reported an inner radius of $r_{\rm in} = 2.08^{+0.17}_{-0.10}\ r_g$.

The new X-ray transient source MAXI J1348–630 was discovered by the MAXI/GSC instrument on 2019 January 26 (Yatabe et al. 2019). The reported position of the source is R.A. = 13:48:12.73, decl. = −63:16:26.8 (equinox J2000.0) with an uncertainty of ∼1.″7 (90% confidence level; Kennea & Negoro 2019) using the Swift XRT observations. After this discovery, all major X-ray observatories such as INTEGRAL, NICER and Insight-HXMT (Chen et al. 2019; Lepingwell et al. 2019; Sanna et al. 2019) conducted follow-up observations to understand the nature of the source. Optical and radio counterparts (Denisenko et al. 2019; Russell et al. 2019) have been reported for the source and the multi-wavelength properties suggested that the source is a BHXRB (Russell et al. 2019; Carotenuto et al. 2021). NICER monitoring observations showed outburst evolution similar to what is commonly observed in BHXRBs and during the outburst phase, the source exhibited different types of quasi-periodic oscillations (QPOs) as well (Belloni et al. 2020; Zhang et al. 2020). Tominaga et al. (2020) reported the analysis of the first half-year MAXI monitoring of the source. In these observations, the source exhibited spectral transitions between the soft and hard states and was consistent with the well-known characteristic of a BHXRB. Assuming a face-on disk around a non-spinning black hole, they estimated the source distance and the black hole mass to be ≈4 kpc and ∼7 $(D/4\ \rm kpc)\ M_\odot$, respectively, and noted that the black hole could be more massive depending on the disk inclination and the spin parameter. Modeling the combined Swift XRT, BAT and MAXI/GSC spectra in the 1–150 keV energy band using the two-component advective flow model, Jana et al. (2020) estimated the black hole mass to be ∼9 $M_\odot$ and the source distance to be 5–10 kpc. Chauhan et al. (2020) studied the H I absorption spectra and obtained a probable distance of $2.2^{+0.5}_{-0.6}$ kpc with a strong upper limit of $5.3 \pm 0.1$ kpc. Later, Lamer et al. (2021) combined data from multiple satellites and used the dust scattering halo to precisely measure the source distance to be 3.39 kpc (with a statistical uncertainty of 1.1%) and a renewed mass estimate for the compact object at $11 \pm 2\ M_\odot$. Using the relativistic reflection model, Jia et al. (2022) fitted the NuSTAR spectra of the source and obtained the spin parameter $a_* = 0.78^{+0.4}_{-0.4}$, and the inclination angle of the inner disk $i = 29.2^{+0.3}_{-0.5}$ degrees. Recently, Kumar et al. (2022) studied the source using the nearly-simultaneous NICER and NuSTAR observations. They estimated the spin, black hole mass and inclination of the source by fixing the distance to 2.2 kpc, and the values were found to be $0.80 \pm 0.02$, $8.7 \pm 0.3\ M_\odot$ and $36.^\circ5 \pm 1.^\circ0$, respectively. Jithesh et al. (2021) used five simultaneous AstroSat and NICER observations for studying the broadband X-ray spectral-timing properties of the source. They noted the presence of QPOs of type-C and type-A classes and further via power density spectrum and energy-dependent root mean square (rms), they confirmed that the disk is significantly less variable than the Comptonization component. They detected hard time lag for the bright hard state in the 0.5–80 keV energy band and modeled the energy-dependent rms and time lag using a single-zone propagation model. They used multi-color disk emission, Gaussian line and thermal Comptonization to identify the spectral states of the observations.

In this work, we study the broadband X-ray spectral characteristics of MAXI J1348–630 considering the same AstroSat observations as used by Jithesh et al. (2021). The primary aim is to constrain the system parameters such as the spin parameter and the inclination angle of the accretion disk using relativistic spectral models. We have utilized data from the LAXPC and SXT payloads onboard AstroSat. Section 2 describes the observations used in this work and the data reduction techniques. The broadband spectral analysis methodology is put forward in Section 3. The main results are discussed in Section 4.

## 2. Observations and Data Reduction

AstroSat (Singh et al. 2014; Agrawal et al. 2017) observed MAXI J1348–630 during its 2019 outburst and we avail five such observations for our study. The details of observations used in this work are given in Table 1.

### 2.1. Large Area X-Ray Proportional Counter (LAXPC)

The Large Area X-Ray Proportional Counter (LAXPC) has three identical proportional counters, namely LAXPC10, LAXPC20 and LAXPC30, functioning in the broad energy band of 3–80 keV with an excellent time resolution of 10 $\mu$s (Yadav et al. 2016; Agrawal et al. 2017; Antia et al. 2017). LAXPC software (LaxpcSoft; version as of 2020 August 4) was used to process the Level-1 Event Analysis (EA) mode data. The data reduction and extraction of science products were carried out using standard tools available in LaxpcSoft. Among the three detectors, LAXPC30 was switched off in 2018 March due to the gas leakage and LAXPC10 was operating at low gain. Thus, we used only the LAXPC20 detector in this study and modeled the spectrum in the 4–25 keV energy band.

**Table 1**
Observation Log

| Data | ObsID | Date | Exposure (ks) | LAXPC (counts $s^{-1}$) | SXT (counts $s^{-1}$) | Radius (arcmin) |
|---|---|---|---|---|---|---|
| Data1 | T03_083T01_9000002722 | 2019 Feb 19–20 | 5.5(L)/1.9(S) | 1535 | 837 | 8 and 16 |
| Data2 | T03_083T01_9000002728 | 2019 Feb 22 | 20.2(L)/11.1(S) | 1492 | 802 | 8 and 16 |
| Data3 | T03_083T01_9000002742 | 2019 Feb 28 | 23.2(L)/12.2(S) | 1130 | 729 | 6 and 16 |
| Data4 | T03_112T01_9000002896 | 2019 May 8–9 | 13.8(L)/6.8(S) | 112 | 13 | 16[a] |
| Data5 | T03_120T01_9000002990 | 2019 Jun 14–15 | 35.0(L)/14.9(S) | 922 | 65 | 2 and 16 |

**Notes.** (1) Data; (2) Observation ID; (3) date of observation; (4) exposure time (L and S represent LAXPC and SXT respectively); (5) LAXPC count rate in the energy range of 4–25 keV; (6) SXT count rate in the 0.8–5 keV energy band; (7) inner and outer radius of the annulus used for extraction of SXT spectrum.
[a] Since the SXT data are not piled-up in Data4 observation, we extracted the SXT spectrum from a circular region of radius 16′.

### 2.2. Soft X-Ray Telescope (SXT)

SXT is an imaging telescope and sensitive to the soft X-ray band, particularly in 0.3–8 keV (Singh et al. 2016, 2017). The SXT observations used in this work are taken in the Photon Counting (PC) mode. Using the SXT pipeline software (version: AS1SXTLevel2-1.4b), we processed the Level-1 data obtained, cleaned the Level-2 event files from different orbits and merged them employing the SXT event merger tool.[4] Four out of five (except Data4) observations had pile-up, which was removed by extracting source events from an annulus region. The extraction radius used for different observations is given in Table 1. We used the blank sky SXT spectrum as the background spectrum and the "sxt_pc_mat_g0to12.rmf" file as the redistribution matrix file. We generated the off-axis auxiliary response files (ARFs) utilizing the `sxtARFModule` tool by giving the on-axis ARF (sxt_pc_excl00_v04_20190608.arf) as input. The individual energy spectra of all these observations were re-binned logarithmically using `grppha`. When modeling the spectra, the gain of the response file is modified by executing the `gain fit` command in XSPEC. The slope at unity was fixed leaving the offset as a free parameter. We modeled the SXT spectrum in the 0.8–5 keV energy range.

## 3. Broadband X-Ray Spectral Analysis

As mentioned in Section 1, Jithesh et al. (2021) characterized the spectral states of MAXI J1348–630 using these same five AstroSat observations. They confirmed that the first three observations (Data1, Data2 and Data3) were in the soft spectral state of BHXRBs, while the last two observations (Data4 and Data5) were in the hard spectral state. In the following two sections, we separately describe the details of the spectral modeling performed on the source in soft and hard states, respectively.

[4] http://www.tifr.res.in/~astrosat_sxt/dataanalysis.html

### 3.1. Soft State Observations

The background-subtracted 3–80 keV LAXPC and 0.3–8 keV SXT light curves of MAXI J1348–630 during its soft state (Data1, Data2 and Data3) are depicted in Figure 1. We performed broadband X-ray spectral analysis using 0.8–5 keV SXT and 4–25 keV LAXPC spectra of each observation. The spectra were analyzed simultaneously by making use of the X-ray spectral fitting software XSPEC version 12.11.1 (Arnaud 1996). Here our aim was to constrain the system parameters: spin ($a_*$), inclination angle of the disk ($i$) and accretion rate ($\dot{m}$). We first employed a phenomenological model consisting of a multi-color disk blackbody (`diskbb`; Mitsuda et al. 1984), a convolution model (`simpl`; Steiner et al. 2009) to represent the Comptonization of disk photons in the inner flow and a Gaussian line profile (`Gaussian`). We relied on the Tuebingen-Boulder Inter-Stellar Medium absorption model (`tbabs`) to account for the Galactic absorption (Wilms et al. 2000). A multiplicative constant was used to address the cross-calibration uncertainties between the SXT and LAXPC instruments. Due to uncertainties in the calibration, 2% model systematic uncertainty was exercised for spectral modeling. The line energy of the Gaussian was fixed at 6.4 keV. The best fit parameters with the errors at 90% confidence level are listed in Table 2.

For taking into account relativistic effects and reflection features, we applied a model which incorporates a multi-temperature blackbody model for a thin accretion disk around a Kerr black hole (`kerrbb`; Li et al. 2005), and the relativistic reflection model (`relxill`; Dauser et al. 2014; García et al. 2014) along with the convolution model (`simpl`). The photon index $\Gamma$ of `relxill` was tied to that of `simpl`. The black hole spin parameter and inclination angle of `relxill` was tied to that of `kerrbb`. The spectral hardening factor and the `kerrbb` normalization were fixed at 1.7 (Shimura & Takahara 1995) and unity, respectively. For `relxill`, the emissivity profile is employed as a broken power law and the emissivity index of the inner and outer part of the accretion disk was frozen at 3. The geometry of the accretion disk is

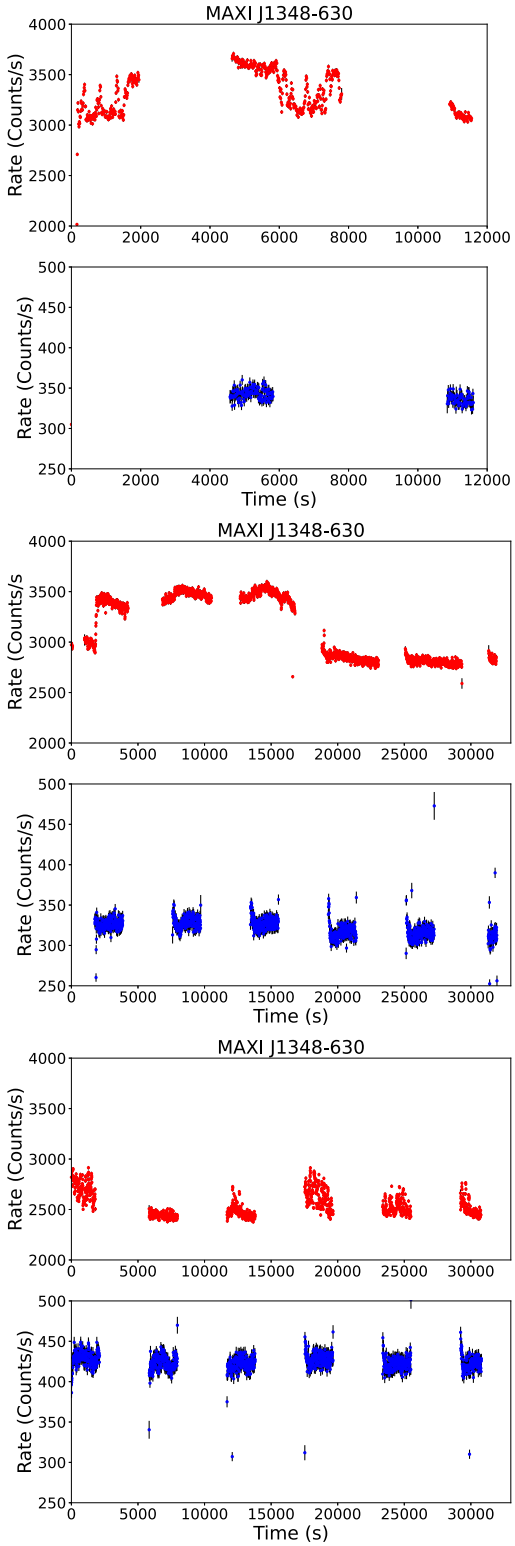


**Figure 1.** The light curves from AstroSat observations in the soft state: Data1 (top), Data2 (middle), and Data3 (bottom). In each plot, the top and bottom panels represent the 3–80 keV light curve from LAXPC20 binned with 10 s and the 0.3–8 keV light curve from SXT, respectively. The reference time for Data1 is MJD 58533, that for Data2 is MJD 58536 and that Data3 is MJD 58542.

described by two parameters: the inner edge of the disk which we assumed at the ISCO and the outer edge of the disk which was frozen to its default value of 400 $r_g$. The redshift of the source was set to zero. The high-energy cutoff was frozen at 70 keV. The material of the disk, also characterized by iron abundance, $A_{Fe}$, is measured in units of iron solar abundance. The ionization of the accretion disk is described by the ionization parameter $\xi$. Lastly, since the output of this model is the reflection spectrum of the accretion disk and the power law component from the corona, there are two parameters to regulate the normalizations of these two components: the normalization of the model and the reflection fraction, which regulates the relative intensity between the reflection spectrum and the power law spectrum. It is frozen to $-1$, thus the output of these models is only the reflection component. Black hole mass and the distance to the source were fixed at 11 $M_\odot$ and 3.39 kpc, respectively, as estimated by Lamer et al. (2021).

The unfolded spectra and residuals from the three soft state observations fitted using `tbabs * (simpl * kerrbb + relxill)` are depicted in Figure 2 and the best fit model parameters are listed in Table 3. We note that the spectral fit parameters do not differ significantly between the observations. In particular, the absorption column density and the photon index seem to be constant at $\sim 6 \times 10^{21}$ cm$^{-2}$ and $\sim$2.0, respectively. The estimated value of black hole spin is constrained to be >0.906 in these observations. The inferred value of inclination angle $i$ varied between 31° and 45°, but was consistent with uncertainties. Comparing the reduced $\chi^2$ from Tables 2 and 3 shows that the fits obtained by these relativistic spectral models are better than the phenomenological models.

The spin parameter, the inclination angle and the iron abundance of the source need to be the same for physical consistency of the fit. For this, we carried out a joint spectral fit for all three observations using `tbabs * (simpl * kerrbb + relxill)`. In the joint fit, the spin parameter, inclination angle and iron abundance were tied between the spectra, whereas other parameters were allowed to vary between the observations. The best fit model parameters are listed in Table 4. Figure 3 shows the confidence contours of disk inclination angle ($i$) and black hole spin parameter ($a_*$). The joint fit yields the spin parameter $0.997^{+0.001}_{-0.006}$, however, we see from Figure 3 that the parameter value is >0.97. Thus, the best fit spin parameter and inclination angle are >0.97 and $32.9^{+4.1}_{-0.6}$ degrees, respectively.

### 3.2. Hard State Observations

The 0.3–8 keV SXT and 3–80 keV LAXPC light curves from hard state observations (Data4 and Data5) are depicted in Figure 4. The spectral analysis of the hard state observations was performed as mentioned in Section 3.1. However, we replaced the `kerrbb` component from the model combination

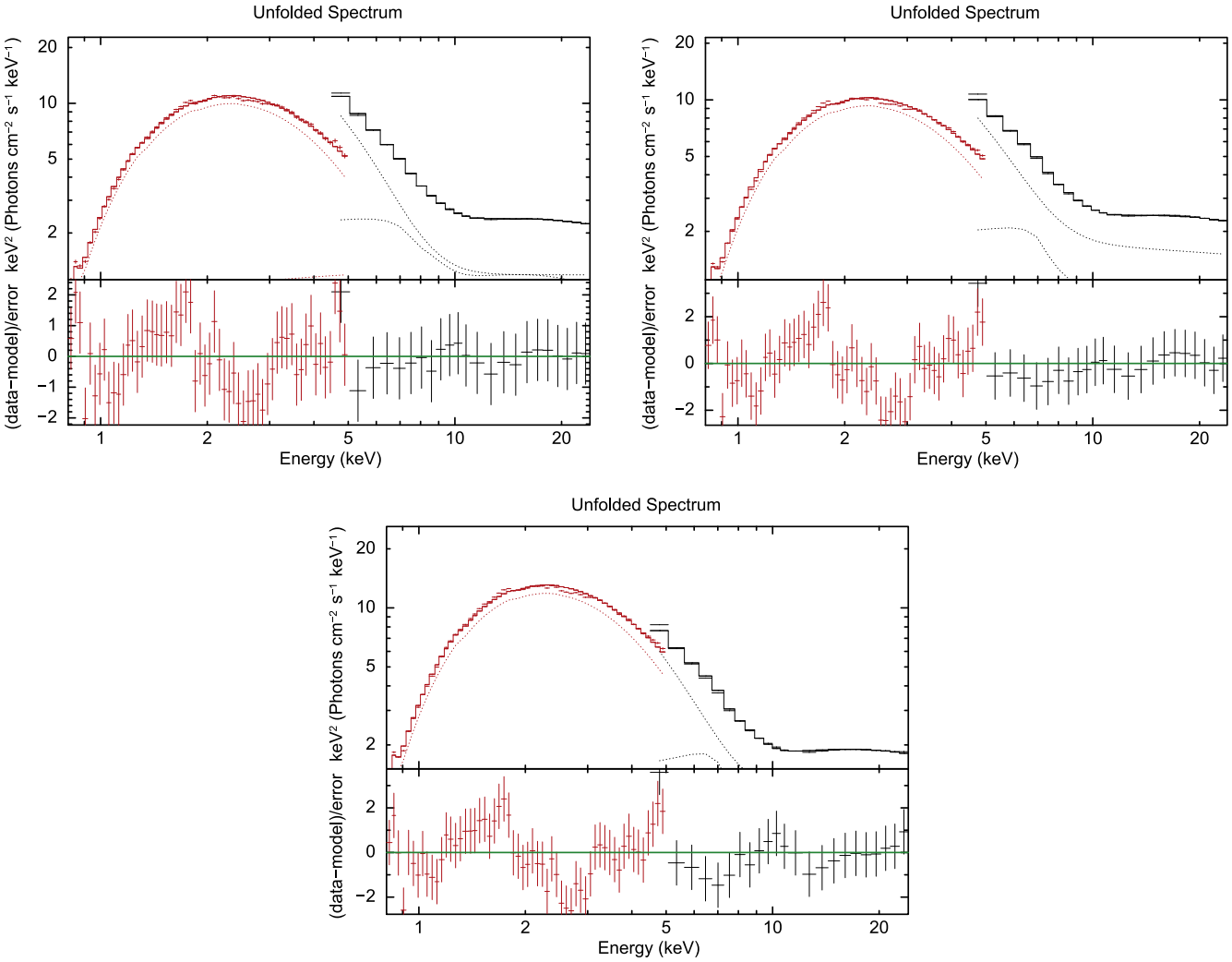


**Figure 2.** The 0.8–25 keV broadband X-ray unfolded spectra of MAXI J1348–630 from Data1 (left), Data2 (right) and Data3 (bottom) observations. The black and red data points represent LAXPC20 and SXT data, respectively. Spectra are fitted with `tbabs * (simpl * kerrbb + relxill)`.

**Table 2**
Broadband X-Ray Spectral Parameters for MAXI J1348–630 from Soft State Observations Fitted with `tbabs * (simpl * diskbb + Gaussian)` Model

| Data | $N_{\rm H}$ | $\Gamma$ | $F_{\rm Sca}$ (%) | $kT_{\rm in}$ | $N_{\rm disk}$ | $\sigma$ | $N_{\rm Gauss}$ | $L_B$ | $\chi^2$/d.o.f |
|---|---|---|---|---|---|---|---|---|---|
| Data1 | $0.53^{+0.01}_{-0.01}$ | $2.01^{+0.06}_{-0.06}$ | $4.9^{+0.5}_{-0.5}$ | $0.82^{+0.01}_{-0.01}$ | $9123^{+713}_{-663}$ | $1.21^{+0.29}_{-0.27}$ | $0.061^{+0.017}_{-0.017}$ | $6.26^{+0.27}_{-0.28}$ | 85.36/73 |
| Data2 | $0.49^{+0.01}_{-0.01}$ | $2.11^{+0.06}_{-0.06}$ | $5.6^{+0.6}_{-0.6}$ | $0.82^{+0.01}_{-0.01}$ | $8514^{+553}_{-589}$ | $1.16^{+0.28}_{-0.26}$ | $0.059^{+0.017}_{-0.017}$ | $5.04^{+0.19}_{-0.20}$ | 120.48/73 |
| Data3 | $0.50^{+0.01}_{-0.01}$ | $2.04^{+0.06}_{-0.06}$ | $4.8^{+0.5}_{-0.4}$ | $0.81^{+0.01}_{-0.01}$ | $7388^{+505}_{-474}$ | $1.19^{+0.23}_{-0.25}$ | $0.049^{+0.013}_{-0.013}$ | $4.79^{+0.05}_{-0.17}$ | 131.07/73 |

**Note.** (1) Data; (2) neutral hydrogen column density in units of $10^{22}$ cm$^{-2}$; (3) asymptotic power law index; (4) scattered fraction of seed photons; (5) black hole spin parameter; (6) inner disk temperature in keV; (7) line width in keV; (8) Gaussian normalization in photons cm$^{-2}$ s$^{-1}$; (9) bolometric luminosity in the units of $10^{37}$ erg s$^{-1}$; (10) statistics and degrees of freedom.

described in Section 3.1 with the relativistic disk model `kerrd` (Ebisawa et al. 2003) to allow for the possibility that the inner disk radius may not be at ISCO. `Kerrd` accommodates the mass, disk inclination angle, accretion rate as well as the inner radius of the disk. The spectral hardening factor, normalization and outer radius of the disk were frozen at 1.7, 1 and $10^4$ $r_g$, respectively. In addition, we fixed the inclination angle, spin parameter and iron abundance to the values obtained from the joint fit of all soft state observations (see Table 4). The inner disk radius of `kerrd` was tied to inner disk radius in

**Table 3**
Broadband X-Ray Spectral Parameters for MAXI J1348–630 from Soft State Observations Fitted with `tbabs * (simpl * kerrbb + relxill)` Model

| Parameter | Data1 | Data2 | Data3 |
|---|---|---|---|
| `tbabs` | | | |
| $N_{\rm H}$ [$10^{22}$ cm$^{-2}$] | $0.62^{+0.01}_{-0.01}$ | $0.61^{+0.01}_{-0.01}$ | $0.59^{+0.01}_{-0.01}$ |
| `simpl` | | | |
| $\Gamma$ | $2.01^{+0.13}_{-0.09}$ | $2.02^{+0.11}_{-0.07}$ | $2.01^{+0.06}_{-0.03}$ |
| $F_{\rm Sca}$ [%] | $2.27^{+1.70}_{-1.11}$ | $2.25^{+1.51}_{-1.03}$ | $2.32^{+0.69}_{-0.73}$ |
| `kerrbb` | | | |
| $a_*$ | $0.961^{+0.024}_{-0.055}$ | $0.994^{+0.004}_{-0.034}$ | $0.997^{+0.001}_{-0.017}$ |
| $i$ [deg] | $38.2^{+7.5}_{-8.4}$ | $32.9^{+4.9}_{-1.7}$ | $34.1^{+4.6}_{-1.0}$ |
| $\dot{m}$ [$10^{18}$ g s$^{-1}$] | $0.52^{+0.12}_{-0.21}$ | $0.37^{+0.09}_{-0.02}$ | $0.29^{+0.07}_{-0.02}$ |
| `relxill` | | | |
| $\log\xi$ [erg cm s$^{-1}$] | $4.13^{+0.23}_{-0.42}$ | $4.11^{+0.22}_{-0.27}$ | $4.02^{+0.05}_{-0.21}$ |
| $A_{\rm Fe}$ | >2.52 | $5.01^{+4.49}_{-2.07}$ | $5.00^{+2.28}_{-1.30}$ |
| norm [$10^{-2}$] | $1.024^{+0.003}_{-0.002}$ | $1.339^{+0.004}_{-0.002}$ | $1.013^{+0.002}_{-0.002}$ |
| $\chi^2/\nu$ | 73.2/71 (1.03) | 99.9/71 (1.41) | 100.9/71 (1.42) |

**Note.** $N_{\rm H}$ is neutral hydrogen column density; $\Gamma$ is asymptotic power law index; $F_{\rm Sca}$ is scattered fraction of seed photons; $a_*$ is black hole spin parameter; $i$ is inclination angle; $\dot{m}$ is effective mass accretion rate of the disk; $\xi$ is ionization of the accretion disk; $A_{\rm Fe}$ is the iron abundance; norm is `relxill` normalization; $\chi^2/\nu$ is $\chi^2$ per degrees of freedom. The values in the bracket are reduced $\chi^2$. The black hole mass and distance to the source are fixed at 11 $M_\odot$ and 3.39 kpc, respectively.

**Table 4**
Broadband X-Ray Spectral Parameters for MAXI J1348–630 from the Three Soft State Observations Jointly Fitted with `tbabs * (simpl * kerrbb + relxill)` Model

| Parameter | Data1 | Data2 | Data3 |
|---|---|---|---|
| `tbabs` | | | |
| $N_{\rm H}$ [$10^{22}$ cm$^{-2}$] | $0.61^{+0.01}_{-0.01}$ | $0.61^{+0.01}_{-0.01}$ | $0.61^{+0.01}_{-0.01}$ |
| `simpl` | | | |
| $\Gamma$ | $2.00^{+0.09}_{-0.06}$ | $1.99^{+0.08}_{-0.06}$ | $2.06^{+0.05}_{-0.09}$ |
| $F_{\rm Sca}$ [%] | $2.15^{+1.34}_{-0.83}$ | $2.02^{+1.32}_{-0.89}$ | $2.89^{+0.94}_{-1.12}$ |
| `kerrbb` | | | |
| $a_*$ | $0.997^{+0.001}_{-0.006}$ | $0.997^{+0.001}_{-0.006}$ | $0.997^{+0.001}_{-0.006}$ |
| $i$ [deg] | $32.9^{+4.1}_{-0.6}$ | $32.9^{+4.1}_{-0.6}$ | $32.9^{+4.1}_{-0.6}$ |
| $\dot{m}$ [$10^{18}$ g s$^{-1}$] | $0.38^{+0.05}_{-0.02}$ | $0.35^{+0.13}_{-0.11}$ | $0.31^{+0.04}_{-0.01}$ |
| `relxill` | | | |
| $\log\xi$ [erg cm s$^{-1}$] | $4.11^{+0.07}_{-0.07}$ | $4.11^{+0.16}_{-0.06}$ | $4.00^{+0.05}_{-0.19}$ |
| $A_{\rm Fe}$ | $5.01^{+2.57}_{-2.33}$ | $5.01^{+2.57}_{-2.33}$ | $5.01^{+2.57}_{-2.33}$ |
| norm [$10^{-2}$] | $1.178^{+0.252}_{-0.237}$ | $1.318^{+0.211}_{-0.212}$ | $1.087^{+0.184}_{-0.172}$ |
| $\chi^2/\nu$ | 285.7/219 (1.31) | | |

**Note.** The black hole mass and distance to the source are fixed at 11 $M_\odot$ and 3.39 kpc, respectively.

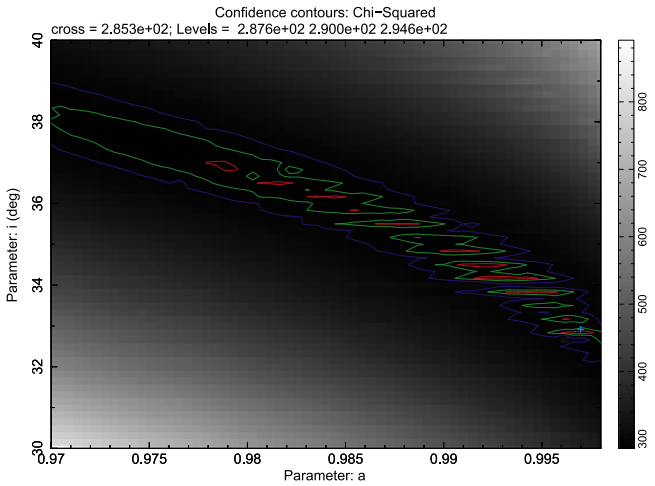


**Figure 3.** Contour plot of the disk inclination parameter ($i$) and spin parameter ($a_*$) of the source from the joint fit of soft state observations. The 68%, 90% and 99% contours are drawn. The plus mark corresponds to the best fit local minimum inferred from the fit.

`relxill` after multiplying by a factor of 1.278, since for `relxill` it is in units of the radius of marginal stability, whereas for `kerrd` the radius is calculated in $r_g$. Note that for $a_* = 0.997$, the radius of marginal stability is 1.278 $r_g$.

The unfolded spectra and residuals for the two observations are depicted in Figure 5 and the best fit model parameters are listed in Table 5. The absorption column density yields $\sim 5 \times 10^{21}$ cm$^{-2}$. The photon index is <1.52 for both observations. The mass accretion rate decreased by an order of magnitude compared to the soft state observations and is $\sim$1–2 $\times 10^{16}$ g s$^{-1}$. The best fit values for $R_{\rm in}$ for Data4 is $\sim$4.9 $r_g$ and hence the disk seems to be truncated. However, for Data5 the radius comes out to be close to ISCO. The $\chi^2$ distributions as a function of $R_{\rm in}$ for Data4 and 5 are displayed in Figure 6. These results are further discussed in the next section.

## 4. Discussion

In this work, we performed detailed broadband spectral analysis of the transient BHXRB MAXI J1348–630 considering AstroSat observations. Using a general relativistic accretion disk and iron line emission along with a thermal Comptonization component, we described the soft state spectra of the source and estimated important system parameters. The joint analysis of soft state observations suggests that the source hosts a rapidly spinning black hole with $a_* > 0.97$. The disk inclination angle, constrained at $i = 32.9^{+4.1}_{-0.6}$ degrees, is consistent with the values reported by Chakraborty et al. (2021).

The three soft state observations are spectrally similar without showing any significant difference in the parameter values (Table 4). On the other hand, Jithesh et al. (2021) report that there are significant differences in the power density

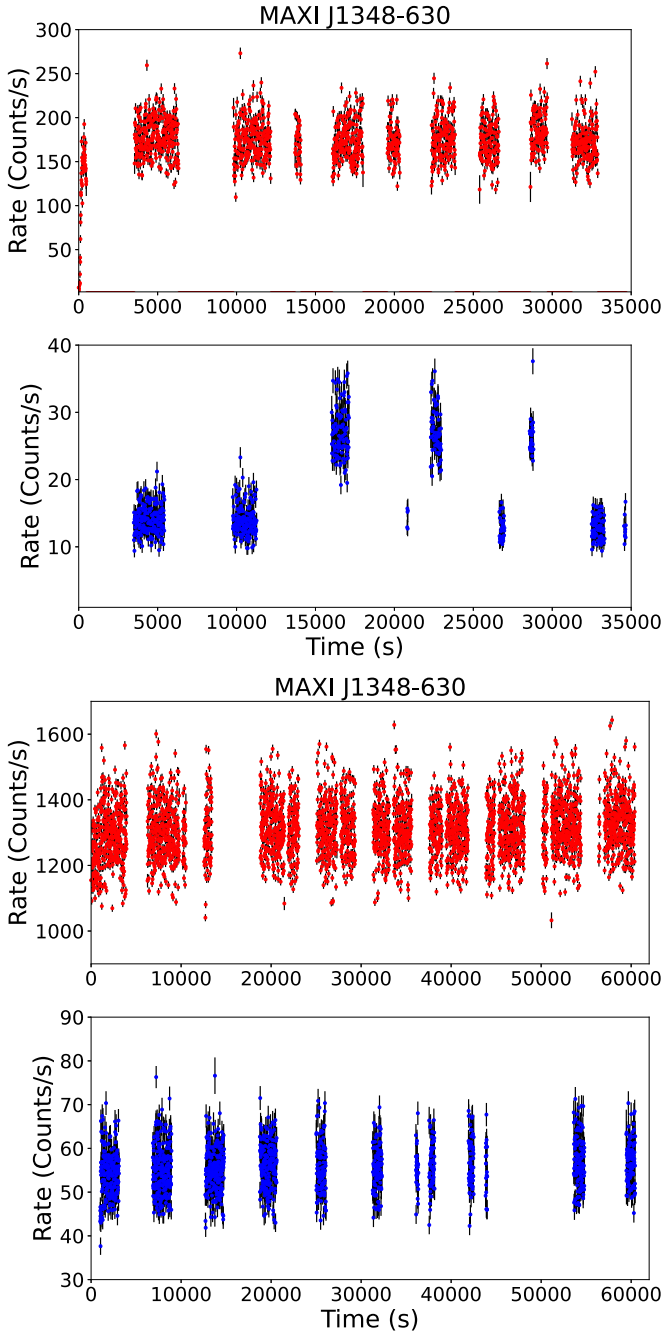


**Figure 4.** The light curves from AstroSat observations in the hard state: Data4 (top) and Data5 (bottom). In each plot, the top and bottom panels represent the 3–80 keV light curve from LAXPC20 binned with 10 s and the 0.3–8 keV light curve from SXT, respectively. The reference time for Data4 is MJD 58611 and that for Data5 is MJD 58648.

spectra of the three observations in the LAXPC (3–15 keV) band. In fact, different segments of Data2 have significantly different variability amplitude. As expected for the soft state, the variability in the NICER (0.5–12 keV) band is significantly

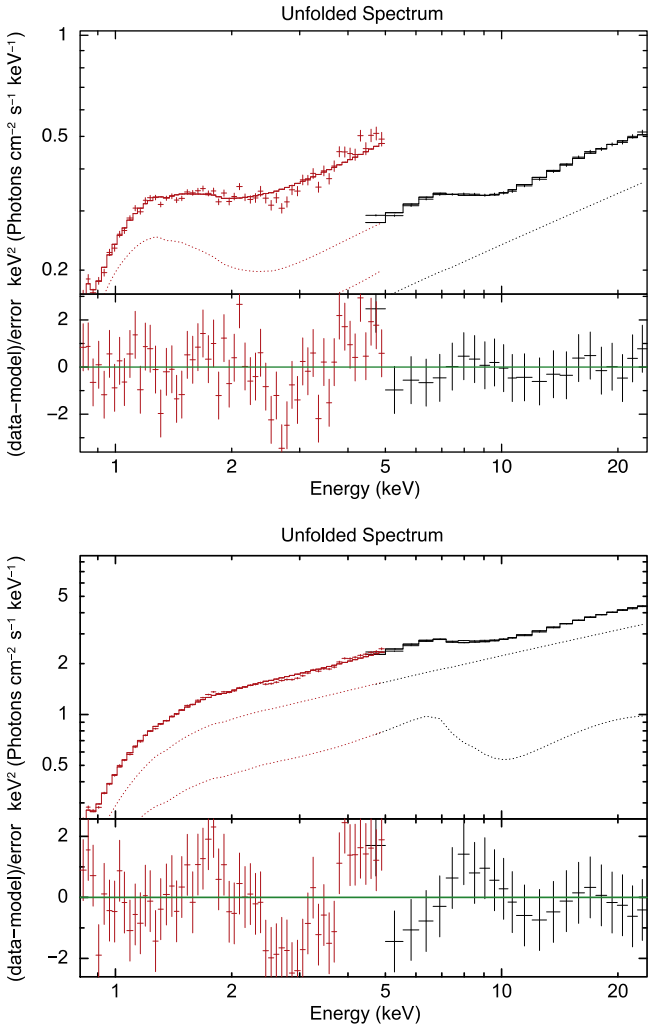


**Figure 5.** The 0.8–25 keV broadband X-ray unfolded spectra of MAXI J1348–630 for Data4 (top) and Data5 (bottom). The black and red data points represent LAXPC20 and SXT data, respectively. Spectra are fitted with `tbabs * (simpl * kerrd + relxill)`.

smaller than that in the higher energy LAXPC band. Thus the disk is relatively stable and the variability that seems to be independent of the disk spectral parameters can be attributed to different temporal properties of the corona.

To better understand the disk truncation in the hard state, we used the relativistic disk model `kerrd` for the hard state observations. For the LHS we obtained a more truncated accretion disk than that for the bright hard state observation. There, the inner radius was estimated to be closer to the black hole. The disk accretion rate was lower by a factor of ten than that of the soft state. Chakraborty et al. (2021) and Kumar et al. (2022) also estimated accretion rates for soft and hard state observations with a difference of a factor of ten. Zhang et al. (2022) too reported an unusual behavior where the inner radius, during the rising hard state, was found to be smaller than in the

**Table 5**
Broadband X-Ray Spectral Parameters for MAXI J1348–630 from Hard State Observations Fitted with `tbabs * (simpl * kerrd + relxill)` Model

| Parameter | Data4 | Data5 |
|---|---|---|
| `tbabs` | | |
| $N_{\rm H}$ [$10^{22}$ cm$^{-2}$] | $0.44^{+0.03}_{-0.04}$ | $0.51^{+0.01}_{-0.01}$ |
| `simpl` | | |
| $F_{\rm Sca}$ [%] | $10.4^{+2.2}_{-1.4}$ | $51.8^{+2.4}_{-2.4}$ |
| `kerrd` | | |
| $\dot{m}$ [$10^{17}$ g s$^{-1}$] | $0.12^{+0.04}_{-0.03}$ | $0.19^{+0.07}_{-0.01}$ |
| `relxill` | | |
| $R_{in}$ [$r_g$] | $4.9^{+1.2}_{-1.1}$ | $1.7^{+2.7}_{-0.3}$ |
| $\Gamma$ | $<1.52$ | $<1.52$ |
| $\log \xi$ [erg cm s$^{-1}$] | $3.8^{+0.3}_{-0.1}$ | $3.4^{+0.1}_{-0.1}$ |
| norm [$10^{-3}$] | $0.44^{+0.05}_{-0.06}$ | $4.14^{+0.11}_{-0.61}$ |
| $\chi^2/\nu$ | 103.2/73 (1.41) | 102.4/73 (1.40) |

**Note.** The black hole mass and distance to the source are fixed at 11 $M_\odot$ and 3.39 kpc, respectively.

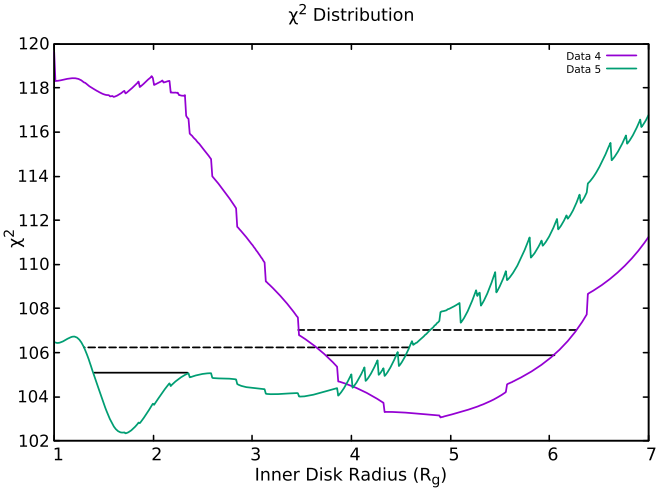


**Figure 6.** The $\chi^2$ distributions as a function of $R_{\rm in}$ when the 0.8–25 keV broadband X-ray spectrum of MAXI J1348–630 is fitted with `tbabs * (simpl * kerrd + relxill)`. The purple and green curves represent Data4 and Data5, respectively. The non-dashed and dashed lines show $3\sigma$ and $4\sigma$ levels respectively.

soft state. In addition, for the bright hard state observation, the estimated unabsorbed bolometric luminosity was lower by a factor of three than that for the soft state, while for the faint hard state observation it was lower, by more than a factor of ten.

An inner disk radius close to the black hole has been reported for the hard spectral state of three other black hole systems: Swift J1753.5-0127, GRS 1739–278 and Cygnus X-1. Miller et al. (2006) analyzed Swift J1753.5–0127 using XMM-Newton and RXTE observations, and reported that the disk remained close to the ISCO in the LHS, during both the rising and decaying phases of the outburst. In the case of GRS 1739–278, NuSTAR observations were conducted during the peak of rising LHS which revealed a broad, skewed iron line and disk reflection spectrum (Miller et al. 2015). Modeling the NuSTAR spectrum with different relativistic reflection models suggested that the accretion disk extends close to the black hole and the estimated inner radius was $\sim 5\ r_g$. In the bright hard state of Cygnus X-1, during the 2014 observations, the disk did not truncate at a large distance from the compact object, instead the disk remained close to the ISCO with an inner radius of $R_{\rm in} < 1.7\ r_{\rm ISCO}$ (Parker et al. 2015). However, Basak et al. (2017) reported the presence of a substantially truncated accretion disk at $\sim$13–20 $r_g$ for Cygnus X-1 by applying a different spectral model. In the case of MAXI J1348–630, we find that the accretion disk extends very close to the black hole with an inner radius of $<2\ r_g$ for the bright hard state observation. Nevertheless, we emphasize that the disk component is weak for the hard state and hence inner radii measurements may be limited by spectral resolution of the instruments and spectral complexity (such as the addition of a low temperature Comptonization component) can affect the estimation (Basak et al. 2017).

MAXI J1348-630 has been observed exhibiting a type-B QPO whose transitions and plausible origins have been studied by several authors. Zhang et al. (2021) and Liu et al. (2022) presented a spectral-timing analysis of the fast appearance/disappearance of a type-B QPO observed in NICER and Insight-HXMT observations of MAXI J1348–630 respectively. Insight-HMXT observed a type-C/B transition that occurs within a very short timescale. Liu et al. (2022) summarized that the variation amplitude (rms) of QPOs increases with energy below 10 keV and remains constant above it from 10 to 100 keV. From their results, they associated the appearance and disappearance of type-B QPO with a change in the flux of the Comptonization component, the inner disk radius and the corona height. They suggest that type-B QPOs probably originate from the precession of the weak-jet in a tilted disk-jet structure located relatively close to the compact object. Zhang et al. (2021) found that the type-B QPO is associated with a redistribution of accretion power between the disk and Comptonized emission. The energy-dependent fractional rms and phase lags of the type-B QPO here have been explained by a two-component Comptonization model (Karpouzas et al. 2020) by García et al. (2021). They gave consideration to the possibility that the variability spectra of the type-B QPO arise from Comptonization occurring in two (a small and a large region) different, but physically connected, regions located in the vicinity of the compact object with a blackbody source of soft photons. They found that the large component dominates the variability below $\sim$2 keV, whereas above that energy the small component prevails in harder energies. Their best fitting

time-dependent Comptonizing model consisted of a small region, with rather low feedback, and a large region, with high feedback. Bellavita et al. (2020) followed the same process using the same model but here the soft photon source is the accretion disk modeled with `diskbb`. Their model `vkdualdk` fits the data very well. Their best fitting model yields a small Comptonization region with very high feedback and a large Comptonization region with a relatively low feedback fraction.

In our study, we reported a difference of more than a factor of six between the luminosities of the bright hard state and the faint one. Furthermore, the accretion rate in the disk is inferred to be lower, while the inner disk radius is larger for the faint state compared to the bright one. Jithesh et al. (2021) reported the rms and time-lag as a function of energy for the hard state observations and modeled them using a single zone Comptonization model (Maqbool et al. 2019). Variations of the inner disk temperature ($\delta kT_{\rm in}$) and the coronal temperature ($\delta kT_e$) occur with a time difference ($\tau_d$) between them which gives rise to the observed energy-dependent rms and time-lag. Jithesh et al. (2021) observed that $\tau_d$ is positive ($\sim$70 ms) for the bright state, but it is negative, $\tau_d \sim -90$ ms, for the faint one when variations at $\sim$1 Hz are considered. This reversal in the sign of the time lag implies that the temporal causality (i.e., whether the disk temperature varies before the coronal temperature or vice versa) changed between the two observations. It is tempting to connect this with the larger inner radius for the faint state suggested in the spectral fitting of this work, however, it is not clear how such a change in geometry will cause the causality to be reversed. Moreover, as mentioned earlier, the estimation of the inner radii during the hard state is subject to uncertainties in the spectral resolution of the instruments and the complexity of the spectral models used to fit the data. Nevertheless, this study underlines the potential of conducting spectral and timing analysis of a black hole system as it evolves through different states using simultaneous observations from different instruments.

## Acknowledgments

We thank the anonymous referee for the constructive comments and suggestions that improved the manuscript. G.M. acknowledges the support from the China Scholarship Council (CSC), Grant No. 2020GXZ016647, and IUCAA Visitors Programme. G.M. would also like to thank Dr. Yash Bhargava for the insightful discussions. V.J. would like to acknowledge the Centre for Research, CHRIST (Deemed to be University), for financial support in the form of a Seed Money Grant (SMSS-2217). The research is based on the observations acquired by the AstroSat mission of the Indian Space Research Organization (ISRO), archived at the Indian Space Science Data Centre (ISSDC). This study has made use of the data whence the LAXPC and SXT instruments. We show courtesy to the LAXPC Payload Operation Center (POC) and the SXT POC at TIFR, Mumbai for dispensing the data from the ISSDC data archive and the imperative software tools. This research has used the data and software provided by the High Energy Astrophysics Science Archive Research Center (HEASARC), which is a service of the Astrophysics Science Division at NASA/GSFC.

## Data Availability

The data used in this work are available in the ISRO's Science Data Archive for AstroSat Mission (https://astrobrowse.issdc.gov.in/astro_archive/archive/Home.jsp).

## ORCID iDs

Gitika Mall https://orcid.org/0000-0003-2426-9808

## References

Agrawal, P. C., Yadav, J. S., Antia, H. M., et al. 2017, JApA, 38, 30
Antia, H. M., Yadav, J. S., Agrawal, P. C., et al. 2017, ApJS, 231, 10
Arnaud, K. A. 1996, in ASP Conf. Ser. 101, Astronomical Data Analysis Software and Systems V, ed. G. H. Jacoby & J. Barnes (San Francisco, CA: ASP), 17
Bardeen, J. M., Press, W. H., & Teukolsky, S. A. 1972, ApJ, 178, 347
Basak, R., Zdziarski, A. A., Parker, M., & Islam, N. 2017, MNRAS, 472, 4220
Bellavita, C., García, F., Méndez, M., & Karpouzas, K. 2020, MNRAS, 515, 2099
Belloni, T. 2009, LNP, 794, 53
Belloni, T. M., Zhang, L., Kylafis, N. D., Reig, P., & Altamirano, D. 2020, MNRAS, 496, 4366
Carotenuto, F., Corbel, S., Tremou, E., et al. 2021, MNRAS, 504, 444
Chakraborty, S., Ratheesh, A., Bhattacharyya, S., et al. 2021, MNRAS, 508, 475
Chauhan, J., Miller-Jones, J. C. A., Raja, W., et al. 2020, MNRAS Lett., 501, L60
Chen, Y. P., Ma, X., Huang, Y., et al. 2019, ATel, 12470, 1
Dauser, T., García, J., Parker, M. L., Fabian, A. C., & Wilms, J. 2014, MNRAS Lett., 444, L100
Denisenko, D., Denisenko, I., Evtushenko, M., et al. 2019, ATel, 12430, 1
Ebisawa, K., Makino, F., Mitsuda, K., et al. 1993, ApJ, 403, 684
Ebisawa, K., Życki, P., Kubota, A., Mizuno, T., & Watarai, K.-y. 2003, ApJ, 597, 780
Fabian, A. C., Rees, M. J., Stella, L., & White, N. E. 1989, MNRAS, 238, 729
García, F., Méndez, M., Karpouzas, K., et al. 2021, MNRAS, 501, 3173
García, J., Dauser, T., Lohfink, A., et al. 2014, ApJ, 782, 76
Gierlinski, M., & Done, C. 2004, MNRAS, 347, 885
Gou, L., McClintock, J. E., Reid, M. J., et al. 2011, ApJ, 742, 85
Homan, J., & Belloni, T. 2005, Ap&SS, 300, 107
Jana, A., Debnath, D., Chatterjee, D., et al. 2020, ApJ, 897, 3
Jia, N., Zhao, X., Gou, L., et al. 2022, MNRAS, 511, 3125
Jithesh, V., Misra, R., Maqbool, B., & Mall, G. 2021, MNRAS, 505, 713
Karpouzas, K., Méndez, M., Ribeiro, E. M., et al. 2020, MNRAS, 492, 1399
Kennea, J. A., & Negoro, H. 2019, ATel, 12434, 1
Kubota, A., & Makishima, K. 2004, ApJ, 601, 428
Kumar, R., Bhattacharyya, S., Bhatt, N., & Misra, R. 2022, MNRAS, 513, 4869
Lamer, G., Schwope, A. D., Predehl, P., et al. 2021, A&A, 647, A7
Lepingwell, A. V., Fiocchi, M., Bird, A. J., et al. 2019, ATel, 12441, 1
Li, L.-X., Zimmerman, E. R., Narayan, R., & McClintock, J. E. 2005, ApJS, 157, 335
Liu, H. X., Huang, Y., Bu, Q. C., et al. 2022, ApJ, 938, 108
Maqbool, B., Mudambi, S. P., Misra, R., et al. 2019, MNRAS, 486, 2964

Miller, J. M., Homan, J., & Miniutti, G. 2006, ApJL, 652, L113
Miller, J. M., Tomsick, J. A., Bachetti, M., et al. 2015, ApJL, 799, L6
Mitsuda, K., Inoue, H., Koyama, K., et al. 1984, PASJ, 36, 741
Motta, S., Muñoz-Darias, T., Casella, P., Belloni, T., & Homan, J. 2011, MNRAS, 418, 2292
Muñoz-Darias, T., de Ugarte Postigo, A., Russell, D. M., et al. 2013, MNRAS, 432, 1330
Muñoz-Darias, T., Motta, S., Stiele, H., & Belloni, T. M. 2011, MNRAS, 415, 292
Parker, M. L., Tomsick, J. A., Miller, J. M., et al. 2015, ApJ, 808, 9
Petrucci, P. O. 2008, MmSAI, 79, 118
Reis, R. C., Fabian, A. C., Ross, R. R., et al. 2008, MNRAS, 387, 1489
Remillard, R. A., & McClintock, J. E. 2006, ARA&A, 44, 49
Reynolds, C. S., & Nowak, M. A. 2003, PhR, 377, 389
Russell, T., Anderson, G., Miller-Jones, J., et al. 2019, ATel, 12456, 1
Sanna, A., Uttley, P., Altamirano, D., et al. 2019, ATel, 12447, 1
Shakura, N. I., & Sunyaev, R. A. 1973, A&A, 500, 33
Shidatsu, M., Ueda, Y., Nakahira, S., et al. 2011, PASJ, 63, S803
Shidatsu, M., Ueda, Y., Yamada, S., et al. 2014, ApJ, 789, 100
Shimura, T., & Takahara, F. 1995, ApJ, 445, 780
Singh, K. P., Stewart, G. C., Chandra, S., et al. 2016, Proc. SPIE, 9905, 99051E
Singh, K. P., Stewart, G. C., Westergaard, N. J., et al. 2017, JApA, 38, 29
Singh, K. P., Tandon, S. N., Agrawal, P. C., et al. 2014, Proc. SPIE, 9144, 91441S
Steiner, J. F., McClintock, J. E., Remillard, R. A., et al. 2010, ApJL, 718, L117
Steiner, J. F., Narayan, R., McClintock, J. E., & Ebisawa, K. 2009, PASP, 121, 1279
Tominaga, M., Nakahira, S., Shidatsu, M., et al. 2020, ApJL, 899, L20
van der Klis, M. 2006, Compact Stellar X-ray Sources, Vol. 39 (Cambridge: Cambridge Univ. Press), 39
Wilms, J., Allen, A., & McCray, R. 2000, ApJ, 542, 914
Yadav, J. S., Misra, R., Chauhan, J. V., et al. 2016, ApJ, 833, 27
Yatabe, F., Negoro, H., Nakajima, M., et al. 2019, ATel, 12425, 1
Zhang, L., Altamirano, D., Cúneo, V. A., et al. 2020, MNRAS, 499, 851
Zhang, L., Altamirano, D., Uttley, P., et al. 2021, MNRAS, 505, 3823
Zhang, S. N., Cui, W., & Chen, W. 1997, ApJL, 482, L155
Zhang, W., Tao, L., Soria, R., et al. 2022, ApJ, 927, 210